Improving the detection limit of conformational analysis by utilizing a dual polarization Vernier cascade

J-W. Hoste,* P. Soetaert, and P. Bienstman

Photonics Research Group (INTEC), Ghent University - imec,
Center for Nano- and Biophotonics (NB-Photonics), Ghent University
Sint-Pietersnieuwstraat 41, 9000 Gent, Belgium

*janwillem.hoste@intec.ugent.be

Abstract: The dual polarization microring technique enables the simultaneous and accurate detection of thickness and refractive index of a bound molecular layer. By using three microring resonators in a double Vernier cascade configuration, the dual polarization technique is improved on three distinct levels: an increase of the sensitivity, a suppression of common noise due to self-referencing and the ability to migrate from a standard tunable laser to a cheap broadband LED and an on-chip arrayed waveguide grating as read-out system, allowing for a system which is orders of magnitude faster and cheaper. A dual polarization Vernier cascade proof-of-concept is fabricated and characterized, a read-out computational framework is constructed and it is shown on a theoretical basis that the limit of detection is improved.

OCIS codes: (130.3120) Integrated optics devices; (140.4780) Optical resonators; (280.1415) Biological sensing and sensors.

References and links

1. R. B. Fenwick, S. Esteban-Martin, and X. Salvatella, "Understanding biomolecular motion, recognition, and allostery by use of conformational ensembles," Eur. Biophys. J. **40**, 1339–1355 (2011).
2. N. S. Hatzakis, "Single molecule insights on conformational selection and induced fit mechanism," Biophys. Chem. **186**, 46–54 (2014).
3. P. R. Connelly, T. M. Vuong, and M. A. Murcko, "Getting physical to fix pharma," Nat. Chem. **3**, 692–695 (2011).
4. A. J. Qavi, A. L. Washburn, J.-Y. Byeon, and R. C. Bailey, "Label-free technologies for quantitative multiparameter biological analysis," Anal. Bioanal. Chem. **394**, 121–135 (2009).
5. S. Janz, D. Xu, M. Vachon, N. Sabourin, P. Cheben, H. Mcintosh, H. Ding, S. Wang, J. H. Schmid, A. Delâge, J. Lapointe, A. Densmore, R. Ma, W. Sinclair, S. M. Logan, R. Mackenzie, Q. Y. Liu, D. Zhang, G. Lopinski, O. Mozenson, M. Gilmour, and H. Tabor, "Photonic wire biosensor microarray chip and instrumentation with application to serotyping of Escherichia coli isolates," Opt. Express **21**, 4623–4637 (2013).
6. P. Adam, J. Dostálek, and J. Homola, "Multiple surface plasmon spectroscopy for study of biomolecular systems," Sensor Actuat. B-Chem **113**, 774–781 (2006).
7. E. Melnik, P. Muellner, R. Bruck, M. Laemmerhofer, and R. Hainberger, "Biofilm growth monitoring on a-si:h based mach-zehnder interferometric biosensors," in "Imaging and Applied Optics Technical Papers," (Optical Society of America, 2012), p. STh1B.4.
8. M. S. Luchansky, A. L. Washburn, T. A. Martin, M. Iqbal, L. C. Gunn, and R. C. Bailey, "Characterization of the evanescent field profile and bound mass sensitivity of a label-free silicon photonic microring resonator biosensing platform," Biosens. Bioelectron. **26**, 1283–1291 (2010).
9. F. Pröll, B. Möhrle, M. Kumpf, and G. Gauglitz, "Label-free characterisation of oligonucleotide hybridisation using reflectometric interference spectroscopy," Anal. Bioanal. Chem. **382**, 1889–1894 (2005).

10. J.-W. Hoste, S. Werquin, T. Claes, and P. Bienstman, "Conformational analysis of proteins with a dual polarisation silicon microring," Opt. Express **22**, 2807–2820 (2014).
11. T. Claes, W. Bogaerts, and P. Bienstman, "Vernier-cascade label-free biosensor with integrated arrayed waveguide grating for wavelength interrogation with low-cost broadband source," Opt. Lett. **36**, 3320–3322 (2011).
12. W. Bogaerts, P. De Heyn, T. Van Vaerenbergh, K. De Vos, S. Kumar, T. Claes, P. Dumon, P. Bienstman, D. Van Thourhout, and R. Baets, "Silicon Microring Resonators," Laser Photonics Rev. **6**, 1–28 (2011).
13. T. Claes, W. Bogaerts, and P. Bienstman, "Experimental characterization of a silicon photonic biosensor consisting of two cascaded ring resonators based on the Vernier-effect and introduction of a curve fitting method for an improved detection limit," Optics Express **18**, 22747–22761 (2010).
14. T. Claes, "Advanced silicon photonic ring resonator label-free biosensors," Ph.D. thesis, UGent (2012).
15. J. C. Mcdonald, D. C. Duffy, J. R. Anderson, D. T. Chiu, H. Wu, O. J. Schueller, and G. M. Whitesides, "General fabrication of microfluidic systems in poly(dimethylsiloxane)," Electrophoresis **21**, 27–40 (2000).
16. D. X. Xu, A. Densmore, A. Delâge, P. Waldron, R. McKinnon, S. Janz, J. Lapointe, G. Lopinski, T. Mischki, E. Post, P. Cheben, and J. H. Schmid, "Folded cavity SOI microring sensors for high sensitivity and real time measurement of biomolecular binding," Opt. Express **16**, 15137–48 (2008).
17. P. De Heyn, D. Vermeulen, D. Van Thourhout, and G. Roelkens, "Silicon-on-Insulator All-Pass Microring Resonators Using a Polarization Rotating Coupling Section," IEEE Phot. Tech. L. **24**, 1176–1178 (2012).
18. PhotonD, http://www.photond.com/products/fimmwave.htm.
19. Luceda, http://www.lucedaphotonics.com.
20. K. De Vos, I. Bartolozzi, E. Schacht, P. Bienstman, and R. Baets, "Silicon-on-Insulator microring resonator for sensitive and label-free biosensing," Opt. Express **15**, 7610–7615 (2007).
21. M. Iqbal, M. A. Gleeson, B. Spaugh, F. Tybor, W. G. Gunn, M. Hochberg, T. Baehr-jones, R. C. Bailey, and L. C. Gunn, "Label-Free biosensor arrays based on silicon scanning instrumentation," IEEE J. Sel. Top. Quant. **16**, 654–661 (2010).
22. S. Pathak, D. V. Thourhout, and W. Bogaerts, "Design trade-offs for silicon-on-insulator-based AWGs for (de)multiplexer applications," Opt. Lett. **38**, 2961–2964 (2013).

1. Introduction

The recognition of the importance of conformation (i.e. shape change) of the actors of a biological binding event is a trend underlined in recent review articles. Fenwick et al. pointed out the relevance of conformation for the analysis of general biomolecular dynamics and molecular recognition [1], while its key role in protein function and regulation has been stressed recently by Hatzakis et al. [2]. Furthermore, Connelly et al. suggest that the difficulties of the pharmaceutical industry to produce new pharmaceuticals the last ten years might be correlated with the poor understanding of the conformational dynamics of proteins which are targeted by possible new drug candidates and the influence of these pharmaceuticals on its conformational behavior [3]. However, the leverage that a better understanding of the conformational aspects of biomolecular interaction could have on the development of new chemicals is not reflected by the available tools to study these subtle dynamics.

Biosensors traditionally measure the amount of bound material by transducing a single signal in a linear domain [4]. By tracking this over time with a high enough resolution, strength of binding, affinity and similar dynamical metrics can be obtained, but conformational changes are largely obscured, at least without making additional assumptions. The most-used technique in drug research still relies on fluorescence detection and hence needs the attachment of a label. While powerful to detect low concentrations of analyte, they are inherently hindered to study conformations due to the sterical hindrance an attached label might induce. Label-free technologies do not suffer from this drawback and hence seem more appropriate to study conformations.

A label-free surface sensing technology that has been receiving a lot of interest lately is based on microring resonators on the Silicon-On-Insulator (SOI) platform. One of the main advantages is that the fabrication tools are shared with the CMOS industry and hence this platform is ready for mass-production at low cost. Furthermore, the microring component is easily stackable in a 2D array such that high throughput can be obtained. Recently, multiplexing of 128 sensors was realized in this manner [5]. Common to integrated optical surface techniques, both

refractive and reflective, is that they interrogate the analytes on the surface with the evanescent tail of an optical mode. This implies that the sensor responds to the optical thickness of the layer which is the product of the refractive index and the thickness. These sensors are in essence blind to shape changes of the attached molecules, which do only change index and thickness, but not their product, i.e. the total bound mass. A multi-color surface plasmon resonance (SPR) technique can circumvent this by exciting the cavity with three wavelengths simultaneously [6]. The downside of this technique is that by interrogating the layer with different wavelengths, the measured absolute characteristics of the molecular layer are prone to dispersive effects, introducing uncertainties. Other integrated surface sensor systems provide information on thickness by growing a large number (>50) of layers and fitting the response of the sensor to simulations in order to obtain the thickness and refractive index of a single layer. This is done for bilayer systems with Mach-Zehnder interferometers [7] and microrings [8]. This technique is interesting for global trends of the layer system, but cannot elucidate the behavior of a single molecular binding layer, since an averaging over many layers is performed. Reflectometric techniques are also used to measure the thickness of thin layers [9], but an assumption needs to be made about the refractive index in order to do so. It is usually assumed that the refractive index of the layer equals the refractive index provided by the manufacturer, but this is only true in the limit of a perfectly dense monolayer. The refractive index of the adsorbed surface layer can indeed differ a lot from this value, which will manifest itself as an error on thickness and reduce the otherwise high intrinsic resolution of a reflective technique.

In [10] we have introduced a different approach by exciting a single microring resonator with two orthogonal modes simultaneously, such that information on thickness and refractive index can be disentangled. A resolution in the order of 0.1 nm on thickness and 1 mRIU on refractive index has been obtained. This technique uses a tunable laser to sweep a span of 10 nm to locate the resonance frequency. As a result the temporal resolution is in the order of 1 second, depending on the speed of the camera. In this work we combine three microring resonators in a dual polarization Vernier cascade in an attempt to enhance the conformational analysis based on dual polarization on three distinct levels. First, the microrings are organized in such a way that the sensitivities of both the TE and the TM mode to a change in the biolayer are enhanced due to the Vernier effect. Second, the system as a whole is made more robust and less susceptible to noise due to the introduction of a self-referencing system. Third, we have adopted a parallel read-out system based on a broadband LED and an integrated arrayed waveguide grating (AWG), suggested by Claes et al. [11], to replace the standard yet expensive serial read-out system based on a tunable laser. This allows us to measure at a higher temporal rate such that fast conformational changes can be quantified. All three of these factors have a positive influence on the limit of detection. Therefore, a theoretical framework is given in order to quantify these advantages numerically and in a comparative manner. A practical design is proposed, fabricated and characterized. A theoretical measurement framework is built in order to extract the thickness and density of a thin layer out of the compound spectra of the dual polarization Vernier cascade. Finally the limit of detection improvement is determined via a theoretical method.

2. Sensor design

2.1. Vernier amplification

The passive structures making up the Vernier cascade are microring resonators [12] fabricated in SOI. The microring consists of a wire waveguide with a silicon rectangular core on top of a silicon dioxide box. There is no side or top cladding. A schematic of the 2D cross section of such a wire waveguide is presented in Fig. 1 (a). The principle of the dual polarization Vernier design is that each polarization has its own tunable Vernier amplification. The configuration of

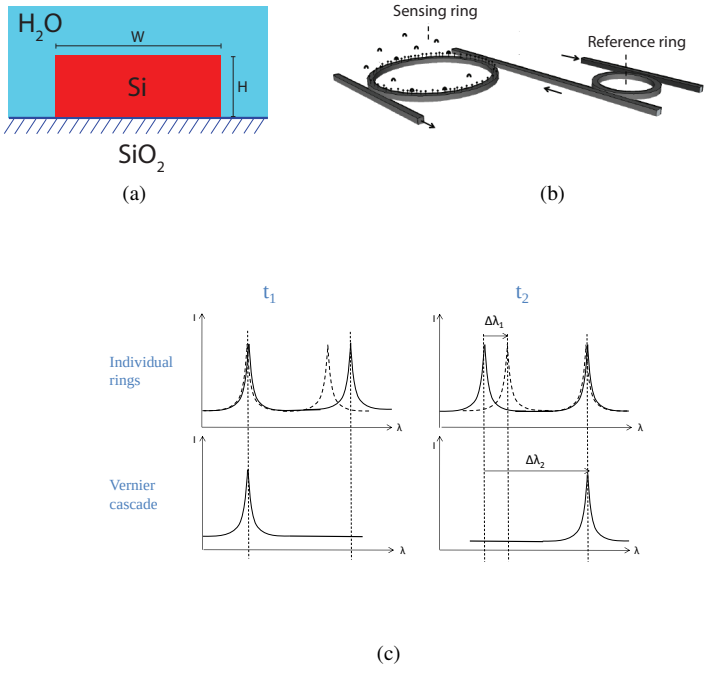

Fig. 1. (a) Cross section of the SOI wire waveguide, consisting of a silicon rectangle of 220 nm high and typically 450 nm wide. (b) Traditional Vernier configuration for a single polarization [14]. (c) Vernier principle: top row shows the spectra of the individual sensing and reference rings in solid and dashed lines before and after a binding event, while the bottom row shows the corresponding Vernier cascade spectrum. At a time t_2 a differential shift $\Delta\lambda_1$ of the individual rings is amplified to a shift $\Delta\lambda_2$ of the Vernier cascade.

a single Vernier amplification has been covered in detail in [13] and consists of two cascaded microring resonators with the drop port of the first ring connected to the input port of the second ring. The drop port of the second ring is then considered the output of the system, as illustrated in Fig. 1(b).

By bonding a microfluidic polydimethylsiloxane (PDMS) cell [15], a fluid containing analytes can be flown over the chip surface through a microfluidic channel. The microring resonators which make up the Vernier cascade are in close proximity and we assume they are subjective to the same collection of fluidic parameters (a.o. geometrical flow conditions, flow rate, temperature, buffer variations, etc). Only one ring is functionalized with receptor molecules however. This ring is the sensing ring, while the ring without probes is the reference ring. In this configuration an amplified response is generated for a differential shift between both rings. Ideally this only occurs during a binding event. This is illustrated in Fig. 1(c), where the top two figures show the output spectra of the individual rings before and after a binding event and the bottom two figures show the corresponding output of the Vernier cascade. We see that the output of the Vernier cascade is maximal when the overlap of the spectra of the two ring resonators is maximal as well. A small shift of the sensing ring $\Delta\lambda_1$ is then transduced to a larger shift $\Delta\lambda_2$ of the Vernier cascade.

This signal amplification is the first advantage of the Vernier cascade and in order to exploit this fully, we formulate two design guidelines for the single polarization case, which we will

have to adhere to for both polarizations in the case of a dual polarization Vernier cascade. The first comes from the fact that Claes et al. [13] have shown that the limit of detection can be greatly improved by moving to a regime where the Vernier output spectrum does not consist of single isolated peaks, as in Fig. 1(c), but out of a comb of peaks whose peak amplitude varies smoothly. The Vernier spectral position is then determined by fitting an envelope to the maxima of the constituent peaks. In order to obtain this comb, we require as a first design guideline that the difference in free spectral range (FSR) between the two rings is small compared to the full width half maximum ($FWHM$) of the resonance peaks of the individual rings [Eq. (1)]. As a second design guideline we strive to maximize the shift amplification of the Vernier cascade (V). This scales with the envelope period of the Vernier cascade ($P_{envelope}$), which in turn is limited by the bandwidth of the grating couplers which couple the light in and out of the SOI chip. Equations (2-4) are the necessary equations to maximize V [13]. Here, λ is the resonance wavelength of the fundamental mode of the microring resonator, L is the length of the resonator and n_g is the group index of the resonator.

$$\Delta FSR < FWHM \tag{1}$$

$$V = \frac{P_{envelope}}{FSR_{sensor}} \tag{2}$$

$$P_{envelope} = \frac{FSR_{sensor} \cdot FSR_{ref}}{\mid FSR_{sensor} - FSR_{ref} \mid} \tag{3}$$

$$FSR = \frac{\lambda^2}{n_g \cdot L} \tag{4}$$

2.2. Single ring equivalent noise reduction

To conceptualize another advantage of the Vernier cascade, the suppression of common noise, we split up the measured wavelength shift of a single ring and of a Vernier cascade in its signal and noise contributions. The noise contributions are in turn split up in optical contributions (alignment, detector noise, noise due to fitting of the spectrum) and buffer contributions (temperature and buffer noise). The superscript V signifies the shift of the envelope of a Vernier cascade, while *ring* stands for the shift of a single ring resonator.

$$\Delta\lambda_{ring} = \Delta\lambda_{ring}^{signal} + \Delta\lambda_{ring}^{noise,opt} + \Delta\lambda_{ring}^{noise,buff} \tag{5}$$

$$\Delta\lambda_{V} = \Delta\lambda_{V}^{signal} + \Delta\lambda_{V}^{noise,opt} + \Delta\lambda_{ring}^{noise,buff} \tag{6}$$

In Eq. (6), we see that the noise contribution due to buffer noise to the envelope shift of a Vernier cascade equals the one to a resonance peak of a single ring resonator. This complies with the fact that for e.g. a temperature fluctuation, both sensing and reference ring are expected to have an equal shift, and hence the Vernier cascade does not amplify this signal but simply shifts with the same amount. The noise contribution due to optical noise to the Vernier shift however, is much larger than the one to a single ring due to the fact that we track an envelope 10-40 nm wide in case of a Vernier cascade, while a single ring has a sharp peak which is only 200 pm wide. For the signal contribution in Eq. (6) we know that $\Delta\lambda_{V}^{signal} = V \cdot \Delta\lambda_{ring}^{signal}$. To evaluate the performance of a Vernier cascade compared to a single ring resonator, we will often make abstraction of the specific sensor system design of the Vernier cascade and use the concept of an equivalent ring resonator. The Vernier cascade will be reduced to a single ring resonator and its improvements will be encoded in physical quantities on the level of a single ring resonator, such as noise, wavelength shift or limit of detection. This is necessary because not only the

sensor system changes, but so does the measurement system, as will become clear in future sections. These equivalent quantities will be indicated by the subscript $*$. Furthermore, to use the Vernier shift of a TE and a TM mode to compute a thickness and density profile, we must calculate the envelope shifts back to the equivalent shift of the single ring resonator as well. This corresponds to $\Delta\lambda^*_{ring} = \Delta\lambda_V/V$. We obtain

$$\Delta\lambda^*_{ring} = \Delta\lambda^{signal}_{ring} + \frac{\Delta\lambda^{noise,opt}_V}{V} + \frac{\Delta\lambda^{noise,buff}_{ring}}{V} \tag{7}$$

Comparing Eq. (5) with Eq. (7), it is clear that the buffer noise is suppressed by a factor V and the total noise contribution depends on the size of the optical noise of the Vernier sensor, which will be addressed further.

The most defining metric to benchmark the performance of a sensor and its measurement system to, is the limit of detection (*LOD*). Hence we will use it to compare the single ring dual polarization sensor to the Vernier cascade dual polarization sensor. Similar to the above, the *LOD* of a single ring will be used, and the *LOD* of a Vernier cascade will be cast to an equivalent single ring *LOD*. The limit of detection is determined by $\Delta\lambda_{min}$ as the minimum detectable wavelength shift, which is a function of the noise contributions, and S as the transduction sensitivity, expressed e.g. in nm/nm and a measure for how much the wavelength shifts for an increase of the thickness of a thin layer. As such, the *LOD* of a single ring is defined as

$$LOD = \frac{\Delta\lambda_{min}}{S_{ring}} \tag{8}$$

We define $\Delta\lambda_{min}$ via the standard deviation of the wavelength noise on a binding curve $\sigma_{\Delta\lambda,ring}$. This can be determined experimentally by tracking the wavelength positions while flowing deionized water over the sensing chip for 10 minutes. The standard deviation on a second order polynomial through these points is regarded as the total noise and amounts to 220 fm for both TE and TM mode. Assuming Gaussian noise and using Eq. (5), we find

$$\sigma^2_{\Delta\lambda,ring} = \sigma^2_{\Delta\lambda,ring,opt} + \sigma^2_{\Delta\lambda,ring,buf} \tag{9}$$

and with Eq. (7), the equivalent ring noise of a Vernier cascade equals

$$\sigma^{*2}_{\Delta\lambda,V} = \frac{\sigma^2_{\Delta\lambda,V,opt}}{V^2} + \frac{\sigma^2_{\Delta\lambda,ring,buf}}{V^2} \tag{10}$$

From Eq. (9), we know that $\sigma_{\Delta\lambda,ring,buf}$ is limited by $\sigma_{\Delta\lambda,ring}$. This means that $\sigma_{\Delta\lambda,ring,buf}$ is smaller than 220 fm and hence negligible towards $\sigma_{\Delta\lambda,V,opt}$ in Eq. (10), which is on the order of 20 pm. Hence, we can approximate

$$\sigma^*_{\Delta\lambda,V} \approx \frac{\sigma_{\Delta\lambda,V,opt}}{V} \tag{11}$$

$$LOD^*_V \approx \frac{\sigma_{\Delta\lambda,V,opt}/V}{S_{ring}} \tag{12}$$

2.3. Design of a dual polarization Vernier cascade

When moving from a single polarization to a dual polarization Vernier sensor, we must adhere to the two design guidelines stated in section 2.1 for each polarization: complying with Eq. (1) and maximizing V. Furthermore, we followed three additional guidelines. First, we have chosen for a design in which as many structures and waveguides are shared as possible, as

Table 1. Design parameters of the TE and TM sensing ring and the TE reference ring: the radius of the microring resonator R, the width of the ring waveguide W_{ring}, the width of the access waveguide W_{acc}, the gap of the coupling section and the coupling length L_c of the coupling section.

	R [μm]	W_{ring} [nm]	W_{acc} [nm]	gap [nm]	L_c [μm]
TE ring	102	450	450	250	12
TM ring	115	600	320	200	10
Ref ring	100	450	450	250	12

opposed to duplicating the single mode design for both modes. Indeed, each time a structure is duplicated, this might introduce extra noise due to fabrication variations on both nominally identical structures. Due to the high index contrast of the SOI platform, small variations in design can have a large impact on system characteristics. We did choose for a separate TE and TM sensing ring so as to relax the complexity of coupling and of the signal processing. This allows the Vernier amplification to be tuned for each mode individually as well. Second, we strive to couple the light in and out of the chip and do all the routing using strictly the TE mode. This way we evade problems with unbalanced powers that arise when using separate routing in both TE and TM mode. Hence, the TM mode only exists inside the microring. Finally, we tried to avoid splitters. Our experience is that splitters might introduce unwanted reflections which can create ripples in the output spectrum, degrading the limit of detection. This does complicate the design on the level of signal analysis, since it is more difficult to isolate certain signals. This will be addressed further.

As a proof-of-concept we designed a dual polarization Vernier cascade which adheres to these five guidelines while maintaining a ring radius of ~100 μm to limit the footprint of the sensor. This stems from purely practical considerations as more sensors can be printed on a single photonic chip for testing purposes this way. It does limit the amplification via Eq. (2). Longer sensors with reduced footprint can be designed however by using folded cavities [16]. The photonic design was fabricated by lithography on SOI wafers by imec through epixfab. Subsequently these wafers are diced into chips and a section of this chip is pictured with SEM and shown in Fig. 2. The reference (TE) sensor resides at the bottom and the two sensing rings at the top, one for TE and one for TM polarization. Since all routing and in- and out-coupling is done in TE mode, we use an asymmetrical coupling section in the TM sensing ring which rotates the TE mode in the access waveguide to a TM mode in the ring waveguide [17]. To obtain this, the waveguide cross sections of the access and ring waveguides as depicted in Fig. 1(b) are designed as follows: the width of the waveguide cross section in the TM ring waveguide is designed to be 600 nm, while the width of the waveguide cross section in the TE access waveguide is 320 nm. All the waveguides have a standard thickness of 220 nm. The reference ring, the TE sensor ring and the routing waveguides are all designed to have a width of 450 nm. Finally, the radii of the three rings are designed to keep footprint reasonable and maximize V_{TE}, which is governed by the reference ring and the TE sensing ring, and V_{TM}, governed by the reference ring and the TM sensing ring. This is done in a way prescribed by Eqs. (2-4), while obeying to Eq. (1) for both polarizations. The group index of the waveguide cross section of the reference ring and the TE sensing ring amounts to 4.36. With a coupling length of the ring of 12 μm and a radius of 100 μm and 102 μm for the reference ring and TE ring respectively, we obtain a ΔFSR of 15 pm. The FWHM of these rings is about 150-200 pm, such that Eq. (1) is fulfilled. Second, the $P_{envelope}$ amounts to 44 nm. With a bandwidth of the grating couplers of 40 nm, the complete envelope can be read out without significant loss of

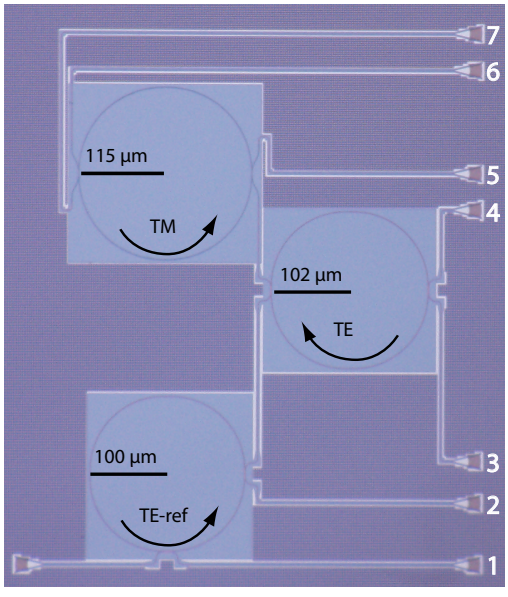

Fig. 2. SEM picture of a dual polarization Vernier design.

power of the outer spectral bands relative to the inner ones. Finally, we design the TM sensing ring to have the same FSR as the TE sensing ring. Similar to the above, this implies a ring radius of 115 μm. The design parameters of this dual polarization Vernier cascade are summarized in Table 1.

2.4. Experimental and theoretical spectra

To characterize the sensor pictured in Fig. 2, light is coupled through the single input port on the left with an Agilent tunable laser through a fiber. Output ports 1, 3 and 7 are read out one by one by sweeping the wavelength of the laser and collecting the light through an optical fiber which is connected to an HP power meter. During the characterization the SOI chip is covered with deionized water to mimic a bio-experiment in which proteins are dissolved in an aqueous buffer and flown over the chip surface. The measured spectra are shown in Fig. 3(a,c,e) for respectively port 1, 3 and 7. In order to verify the experimentally obtained spectra, the sensor is simulated through a combination of the commercially available packages Fimmwave [18] and Caphe [19]. Fimmwave is a mode-solver which is used to solve the 2D cross section, providing us with n_{eff} and n_g of the TE and TM mode. This data is fed into Caphe which is a novel photonic circuit modeler, designed by Luceda. It allows to connect the rings and generate the output spectra at the three output ports. The simulated output spectra are shown in Fig. 3(b,d,f) for respectively port 1, 3 and 7.

We can see that the measured spectrum of port 3 agrees to the simulated spectrum of port 3 very well. The measured period amounts to 45.15 nm, close to the designed period of 44 nm. Although the period of the simulated spectrum of port 7 differs from the one in the measured spectrum, the shape bears close resemblance. This is due to the fact that the fabrication tolerances will only have a small influence on the spectrum of port 3 compared to port 7, since the cross sections of the reference ring and the TE sensing ring are equal. A bias will hence have a minor effect due to the relative nature of the Vernier cascade. On the contrary, port 7 is a combination of 2 different cross sections, as well as 2 orthogonal polarizations. While the TE

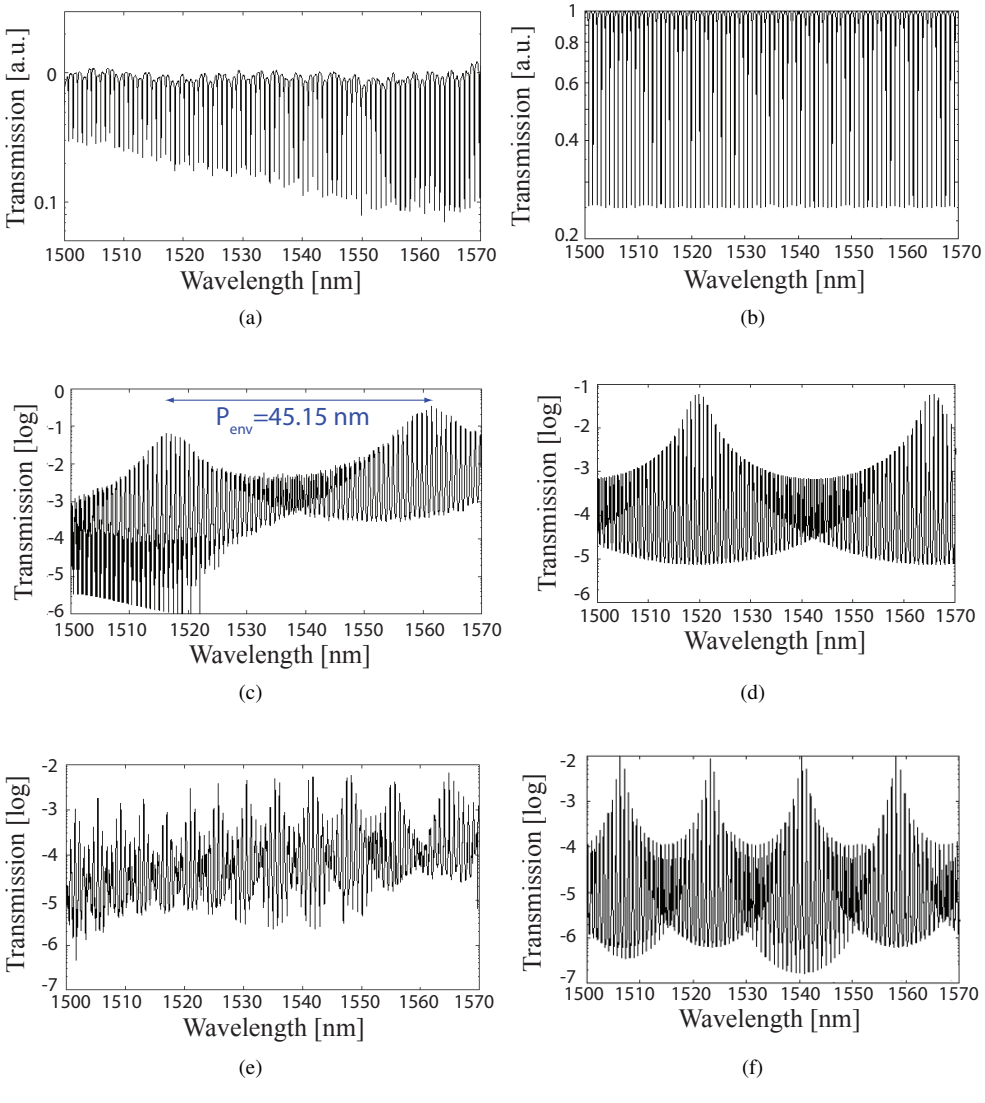

Fig. 3. Simulated and measured spectra of the output ports of the Vernier cascade, with the port numbers shown in Fig. 2. (a) Measured spectrum of port 1, (b) simulated spectrum of port 1. (c) Measured spectrum of port 3, (d) simulated spectrum of port 3. (e) Measured spectrum of port 7, (f) simulated spectrum of port 7. The measured spectra are compensated for the transmission spectrum of the grating coupler.

mode is more sensitive to changes in the width, the TM mode is more sensitive to changes to the height. Due to the relative flatness of the waveguide, the TM mode is more sensitive to fabrication tolerances and thus the spectrum at port 7 is expected to differ more from simulations than the spectrum at port 3.

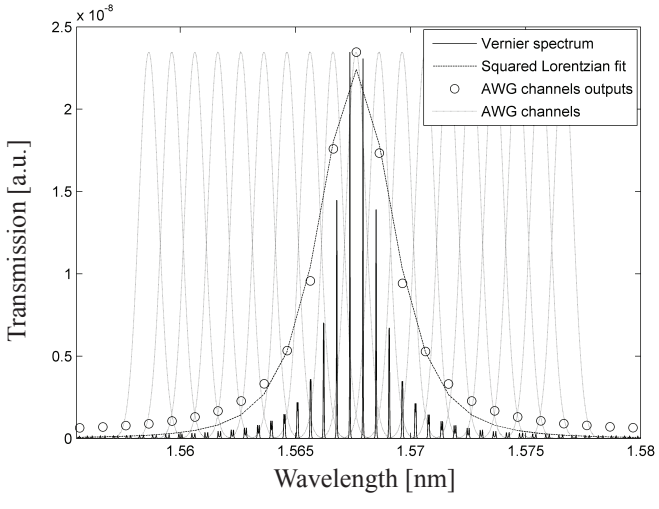

Fig. 4. Vernier spectrum convolved with a Gaussian AWG channel of 0.5 nm wide. Through the sampled discrete points, a squared Lorentzian is fit to determine the peak position.

2.5. Including an AWG to improve the limit of detection

As mentioned in the introduction, the rationale of exploring the presented sensor is improving the limit of detection due to an increase in sensitivity and a decrease of the contribution of noise on the measured signal. The amplification of the resonance shift due to the Vernier effect has a third major advantage however: it allows to discard the expensive tunable laser in the measurement system and swap it for a cheap broadband LED.

In order to track the shift of a resonance feature of any cavity sensor, the spectral resolution of the measurement system needs to be fine enough to resolve the resonance feature. For a single microring resonator, this means the system needs to cope with the stringent spectral requirements of a 100-200 pm wide resonance peak. The standard way of doing this is by leveraging the fine spectral sampling of a tunable laser source (~5 pm), combined with a spectrally blind power meter [20, 21]. Eq. (2) shows that the resonance feature of a Vernier cascade that needs to be tracked (P_{env}) scales with the amplification factor V. In practice, the envelope is 10-40 nm wide, such that the width of the feature we track increases over a hundred-fold, compared to a single ring. By increasing the spectral resolution of the measurement system by the same amount to 0.5 nm, we should thus not experience any deterioration of the limit of detection of the sensor due to undersampling. This spectral feature is in the ballpark of an integrated AWG, which can have a channel width down to 0.5 nm [22]. This leads to the conclusion that we can flip the measurement system around, with regards to where the spectral filter is located: a spectrally blind broadband LED as input, and an integrated spectral filter (AWG) with off-chip detectors on a camera as output. Since every wavelength channel has its own waveguide, output coupler and also a dedicated pixel on the camera, this system captures the whole spectrum in one camera frame. In Fig. 4 we see how a Vernier spectrum is sampled by an AWG and subsequently an envelope is fit through these sampled points to determine the central position. One major advantage of this scheme is that the full spectrum can now be captured at the rate of the camera, while for the sequential system with a tunable laser that is swept, a single camera

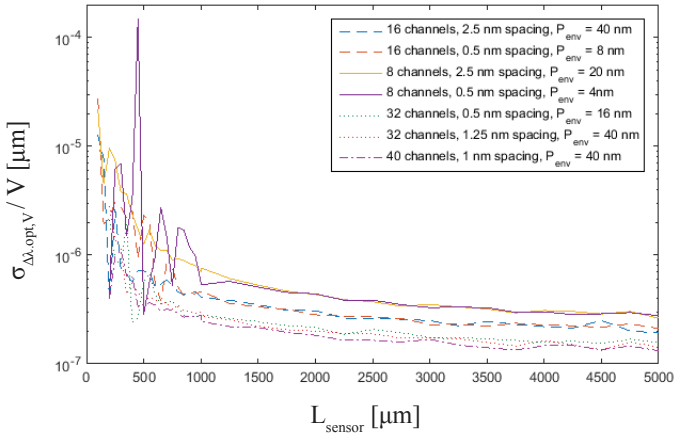

Fig. 5. Classical limit of detection in function of the length of the sensor ring in a single polarization Vernier cascade for several AWG designs.

frame is used for a single wavelength. For a span of 10 nm with a 5 pm resolution, the new system is therefore 2000 times faster. In absolute terms, a 1D line camera can have a framerate surpassing 20 kHz, paving the way for a very high temporal resolution system. Furthermore, a broadband LED costs a fraction of a tunable laser, which is by far the dominant cost factor in the whole system.

To benchmark the influence of the parameters of an AWG such as number of channels and channel spacing we shall use the limit of detection as determined in Eq. (12). Since S_{ring} is not influenced by the addition of an AWG, only the determining fraction $\sigma_{\Delta\lambda,V,opt}/V$ is plotted in function of the length of the sensor ring for a single polarization Vernier cascade in Fig. 5. Several AWG designs with varying number of channels and channel spacings are included. We have set the envelope period of the Vernier spectrum equal to the number of channels multiplied by the channel spacing. The noise on the binding curve which determines the *LOD* is computed via Monte Carlo simulations. For each value of L_{sensor}, the corresponding L_{ref} is determined via Eq. (3). Next, the theoretical Vernier spectrum is obtained via its two theoretical microring spectra [12]. This Vernier spectrum is then convolved with the AWG channel profile, as shown in Fig. 4. Additionally, relative intensity noise with a 0.01 standard deviation and a fixed noise floor with a 0.01 standard deviation is added in an uncorrelated way to each of the discrete points of this spectrum to represent noise in the optical alignment and detector noise. These parameters correspond to measured noise values. Finally, this discrete noisy spectrum is fit to a squared Lorentzian [13] to determine the peak position. For each value of L_{sensor}, this is repeated 500 times with the normally distributed noise quantified above. The standard deviation on these 500 peak positions can be regarded as the optical noise $\sigma_{\Delta\lambda,opt,V}$. This noise is divided by the sensitivity enhancement V [Eq. (2)] to obtain a metric that scales with the LOD.

From Fig. 5 we can conclude first that the LOD improves when the sensor gets longer. This is to be expected since the amplification scales with the length of the sensor, for a constant envelope period. The improvement in LOD saturates however, which is due to the broadening of the Vernier cascade for longer sensors. Furthermore, as the single sensor peaks get closer together they can start overlapping which causes the Vernier spectrum to diminish in contrast. Both spectral broadening as well as a loss in contrast have a negative impact on $\sigma_{\Delta\lambda,opt,V}$. An optimal length of 4 mm is observed. With a maximal P_{env} of 40 nm, this corresponds to a

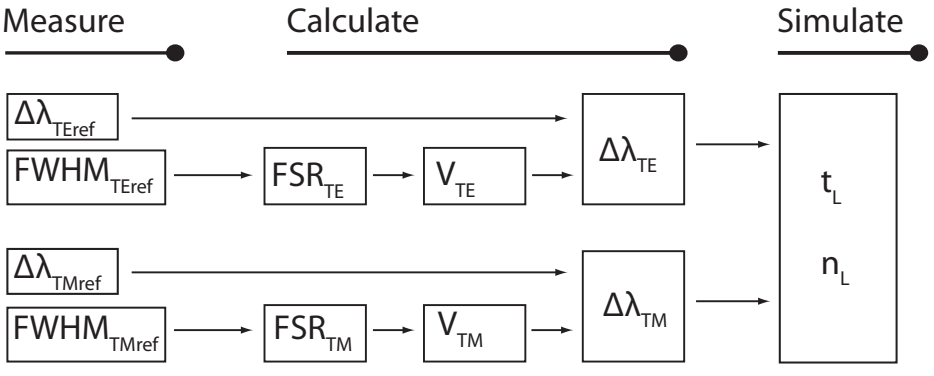

Fig. 6. Measurement framework to determine the thickness and refractive index of a bound molecular layer to the surface of the microrings making up the dual polarization Vernier cascade.

maximal V of 288 [Eq. (2)]. Second, an increase in the number of channels clearly has a positive influence on the LOD. This causes a better sampling of the Vernier cascade and a reduction of $\sigma_{\Delta\lambda,opt,V}$. Third, for a given sensor length and number of channels, increasing the envelope period does not have an influence. The sensitivity increase accompanied by an increase in P_{env} is canceled out by an equal increase of $\sigma_{\Delta\lambda,opt,V}$ due to an increase in channel spacing.

3. Measurement framework

The presented technique is used to measure the thickness (t) and the refractive index (n) of a biomolecular layer bound to the surface of a microring resonator with higher precision than before. This requires that we devise a measurement framework which extracts the effective indices, or equivalently, the resonant wavelength shifts of the microring resonators from the measured Vernier cascade spectra. In a previous publication we have shown how these resonance wavelength shifts can then be used to calculate t and n unambiguously [10]. This measurement and calculation framework is presented schematically in Fig. 6. The spectra at port 3 and port 7 as indicated in Fig. 2 are continuously collected at the framerate of the camera. Fitting these spectra to a squared Lorentzian allows us to determine the shift $\Delta\lambda^{env}_{TEref}$ and the FWHM of the envelope $FWHM^{env}_{TEref}$ of the TE mode at port 3 and $\Delta\lambda^{env}_{TMref}$ and $FWHM^{env}_{TMref}$ of the TM mode at port 7. The FWHM's are used to determine the FSR of the resonance peaks of the individual TE and TM rings via the following equation, which is derived in detail in [13]:

$$FWHM^{env} = 2 \cdot \sqrt{\sqrt{2}-1} \cdot \frac{FWHM_{ring} \cdot FSR_{min}}{|FSR_{ref} - FSR_{sensor}|} \tag{13}$$

FSR_{sensor} denotes the said FSR of the individual TE or TM rings, while FSR_{ref} denotes the FSR of the reference ring. $FWHM_{ring}$ equals FWHM of the TE ring in case the envelope consists of the TE ring and the reference ring and equals in close approximation the geometrical mean of the FWHM of the TM ring and the reference ring in case the envelope consists of a combination of the reference ring and the TM ring. $FWHM_{ring}$ can be considered constant during the experiment, as well as FSR_{ref} for small noise factors in a certain bulk fluid. Once FSR_{sensor} has been determined, the Vernier amplification can be determined via Eqs. (2-3). Finally the shifts $\Delta\lambda^{env}_{TEref}$ and $\Delta\lambda^{env}_{TMref}$ can now be divided by their respective amplification factors to retrieve

the shifts of the individual TE and TM rings $\Delta\lambda_{TE}$ and $\Delta\lambda_{TM}$, which can be calculated back to a thickness and refractive index of the layer-under-test.

4. Sensor performance

4.1. Detection limit of a system with two unknowns

The limit of detection for a system with two unknowns (t and n) is less straightforwardly defined as for a system with one unknown. In the latter case, if we use a microring with a single polarization we can link the change in resonance wavelength to a change in a single parameter by calibrating the system. This single unknown parameter can e.g. be the thickness t of a bound layer, at which point we must assume the refractive index n:

$$\Delta\lambda_{TE} = S \cdot t \tag{14}$$

By virtue of calibration, the system is now represented by a single scalar S, such that the limit of detection, as the thinnest layer we can measure, is simply defined by inverting this system and Eq. (8) is trivial, as this action of inverting is a division. For a two-equation system with two unknowns however, we chose to use Maxwell's equations to obtain a non-linear analytical expression for both measurable quantities ($\Delta\lambda_{TE}$ en $\Delta\lambda_{TM}$) in t and n:

$$\Delta\lambda_{TE} = f(t,n) \tag{15}$$

$$\Delta\lambda_{TM} = g(t,n) \tag{16}$$

When a certain $\Delta\lambda_{TE}$ and $\Delta\lambda_{TM}$ are measured, the above two equations give rise to two curves in the (t,n)-space. The intersection point of these curves determines the thickness and refractive index of the thin layer. This procedure is illustrated in Fig. 7. Instead of linearizing this system such that an inverse can be determined providing us with a similar LOD procedure as for the system defined by Eq. (14), we chose a different approach which does not give rise to linearization errors. The limit of detection on t and n is determined by adding and subtracting $\sigma_{\Delta\lambda,ring}$ [Eq. (9)] to the measured shifts in the left-hand side of Eqs. (15-16): $\Delta\lambda_{TE} \pm \sigma_{\Delta\lambda,ring}$ and $\Delta\lambda_{TM} \pm \sigma_{\Delta\lambda,ring}$. These 4 sets of 2 equations provide 4 unique solutions in the (t,n)-space that delineate the error area as indicated in Fig. 7. The width and height of the error area define the limit of detection of t and n. The noise factor $\sigma_{\Delta\lambda,ring}$ is determined in section 2.5 to be 220 fm for both modes.

4.2. Theoretical detection limit of a Vernier cascade

In order to assess the limit of detection for both t and n for the Vernier cascade, we need to use the same protocol as in the previous section, but we replace $\sigma_{\Delta\lambda,ring}$ by the ring equivalent noise factor of the Vernier cascade $\sigma^*_{\Delta\lambda,V}$ as determined in Eq. (11). This allows us to preserve the ring resonator equations $f(t,n)$ and $g(t,n)$. Equation (11) shows that this requires us to determine the optical noise of a Vernier cascade sensor $\sigma_{\Delta\lambda,V,opt}$ and divide it by the Vernier amplification factor V. This is done by performing Monte Carlo simulations similar to the one in section 2.5, but with a sensor length of 4 mm, as we found (in section 2.5) that this is the optimal sensor length. We have set the envelope period to 32 nm, while choosing an AWG spectrum which is 40 nm wide. This is to prevent the peak of the Vernier envelope to just coincide with the edge of the AWG width, rendering the fitting impossible. The envelope period and sensor length fix the sensitivity enhancement to 231. Different than the previous Monte Carlo simulation is that the design of the Vernier and AWG is fixed, but the position of the Vernier, relative to the AWG is shifted for every iteration, corresponding to a realistic sensing experiment. The noise parameters are equal to those in section 2.5. The standard deviation is now determined on the error

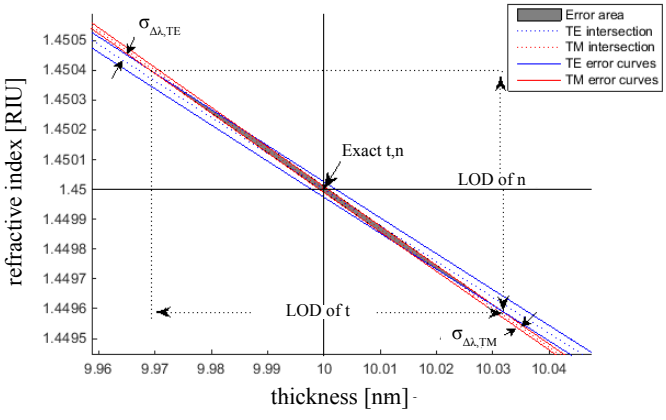

Fig. 7. Visualization of solving procedure in (t,n)-plane to determine t and n from $\Delta\lambda_{TE}$ and $\Delta\lambda_{TM}$. The influence of $\sigma_{\Delta\lambda,TE}$ and $\sigma_{\Delta\lambda,TM}$ on the determination of the limit of detection of t and n also becomes apparent via the indication of the error area.

Table 2. The table is subdivided in three parts, separated by double vertical lines. In the first part, the parameters of the optimized design of the Vernier cascade with AWG are given as the amount of AWG channels, the AWG channel spacing, the length of the sensor ring L_{sensor}, the period of the Vernier envelope P_{env} and the Vernier amplification factor V. The second part shows the simulated optical noise of this configuration obtained via Monte Carlo simulations as the optical noise $\sigma_{\Delta\lambda,opt,V}$ and the ring equivalent optical noise $\sigma^*_{\Delta\lambda,V}$. In the rightmost part, the average theoretical detection limit on refractive index and thickness obtained with this system is given as LOD_n and LOD_t.

AWG [channels×spacing]	L_{sensor} [μm]	P_{env} [nm]	V	$\sigma_{\Delta\lambda,opt,V}$ [pm]	$\sigma^*_{\Delta\lambda,V}$ [pm]	LOD_n [mRIU]	LOD_t [pm]
[40×1] nm	4 mm	32	231	37.22	0.161	0.84	28.9

of the peak position for 5000 iterations. For the optimum Vernier cascade and AWG design we find an optical noise $\sigma_{\Delta\lambda,V,opt}$ of 37.2 pm. Dividing this by V, we obtain that $\sigma^*_{\Delta\lambda,V}$ equals 161 fm. Since this is smaller than the $\sigma_{\Delta\lambda,ring}$ of 220 fm, we expect the 2D limit of detection to decrease. This ring equivalent noise can be used to compute the theoretical limits of detection LOD_t and LOD_n as shown in Fig. 7. We repeat this procedure for a 2D space of (t,n)-couples in the domain [2 nm; 10 nm] × [1.43; 1.47], representing realistic layers of proteins. The average LOD_t amounts to 28.9 pm and the average LOD_n amounts to 0.84 mRIU. The parameters of this Vernier+AWG configuration, the simulated noise characteristics and the theoretical detection limit for thickness and refractive index are summarized in Table 2. When the same procedure is done with the measured 220 fm for a single ring, we find an average LOD_t of 39.6 pm and an average LOD_n of 1.1 mRIU.

This shows that a small improvement in LOD is made over a single dual polarization ring. However, the system has become orders of magnitude cheaper, and the time resolution has

increased by 2000 times. This increased time resolution can be beneficial to observe fast conformational changes, but it can also be used to improve the limit of detection even further by averaging. A signal with uncorrelated gaussian noise with variance σ can be downsampled by a factor M by replacing M samples by its average. This downsampled signal has a reduced variance of $\sigma/\sqrt{M}$. If we reduce the time resolution of the Vernier cascade to the time resolution of a single ring resonator via downsampling, we can now rewrite Eq. (12) as follows, with downsampling factor M equaling to the ratio of the temporal rates ($R_V/R_{ring} = 2000$):

$$LOD_V^* \approx \frac{\sigma_{\Delta\lambda,V}^*}{\sqrt{R_V/R_{ring}}} \cdot \frac{1}{S_{ring}} \tag{17}$$

The first factor on the right-hand side equals 3.6 fm, such that with a similar routine as in Fig. 7, the average LOD_t amounts to 0.6 pm and LOD_t amounts to 17.9 μm. These numbers are unrealistic however since for fast enough rates, the noise will no longer be Gaussian nor uncorrelated and hence the σ will no longer decrease by averaging. As such, these numbers are a strict theoretical limit. This last section does show that an improvement in the limit of detection is possible by using a system with a higher acquisition rate. The size of this increase is however subject to a detailed noise analysis and measurements, which is beyond the scope of this paper. Additionally, biosensor experiments with real biomolecules will be performed in future work.

5. Conclusion

We have designed and fabricated a Vernier cascade dual polarization sensor and have shown that a theoretical improvement in performance is expected compared to a single ring dual polarization sensor. The functionality remains the conformational analysis of proteins through simultaneous determination of thickness and refractive index of a thin molecular layer which binds to the sensor surface. However, by using a compound sensor consisting of three rings, three main advantages were found: an increased sensitivity due to the Vernier amplification, a reduction of common noise factors due to self-referencing and the possibility to employ a measurement system comprising of a cheap LED and an on-chip AWG as a spectral filter. This last advantage allows to measure conformational changes at a rate which is increased by factor of 2000 and at a cost which is orders of magnitude smaller compared to the standard way of measuring ring resonators by sweeping an expensive tunable laser. We have fabricated a proof-of-concept of the sensor and were able to match the measured spectra at the several output ports to simulated spectra. We have used these theoretical spectra to propose a measurement and computational framework to obtain the thickness and density of the bound molecular layer based on the measured compound spectra. Furthermore, we have proposed an optimal design, both with respect to the microring parameters of the Vernier cascade as to the parameters of the AWG. The limit of detection of the Vernier cascade + AWG has been determined theoretically in a way that allows direct comparison to the dual polarization single ring resonator. As such an improved limit of detection of 28.9 pm on thickness and of 0.84 mRIU on refractive index has been obtained. Finally, it has been shown that the limit of detection can be further improved compared to a single ring resonator by leveraging the increased temporal rate due to the parallel read-out of the spectrum.